Journal of the Taiwan Institute of Chemical Engineers 135 (2022) 104369

Contents lists available at ScienceDirect

Journal of the Taiwan Institute of Chemical Engineers

journal homepage: www.elsevier.com/locate/jtice

Flow transition of magnetohydrodynamic bubbly jet driven by Lorentz force

Jia-Hong Cheng, Li-Wei Cheng, Ching-Yao Chen*

Department of Mechanical Engineering, National Yang Ming Chiao Tung University, Taiwan R.O.C., 1001 University Road, Hsinchu, Taiwan 300, R.O.C.

ARTICLE INFO

Article History:
Received 2 December 2021
Revised 12 April 2022
Accepted 5 May 2022
Available online xxx

Keywords:
MHD Jet
Lorentz force
Reynolds number
Turbulence breakup

ABSTRACT

Background: Magnetohydrodynamic (MHD) jet in saltwater possesses potential applications to improve marine vehicle propulsion and hydrogen collection. In the present paper, pattern and flow transition of MHD bubbly jets are studied. Bubbles of oxygen and hydrogen, produced by electrolysis in saltwater and displaced by the Lorentz force, form a typical multiphase MHD jet flow.

Methods: Taking advantage of the brightness of gaseous bubbles, emergence of bubbly jet can be directly observed. Pattern of the bubbly jet is experimentally confirmed to resemble the saltwater jet, and used for further analysis.

Findings: A Lorentz-force based Reynolds number Re_L is proposed to demonstrate the pattern similarity of the MHD jet, and thus applied to categorize the transition of flow regimes from laminar to turbulent. For a jet of lower Re_L, the pattern of the bubbly jet appears as a continuous, wavy and laminar stream. Turbulent breakups start to evolve at farther downstream of the bubbly jet once the Re_L exceeds a critical value. The critical value of $Re_L \approx 1500$ is verified both by visual observation and relevant quantitative measures of the bubbly jet.

1. Introduction

Magnetohydrodynamic (MHD) concerns the dynamics of conducting or magnetic fluids driven by magnetic and electric fields. A branch of MHD is driving conducting fluids, e.g., plasma, liquid metal and saltwater etc., by the Lorentz force generated by perpendicularly placed magnetic field and electric current. Applications of this particular branch of MHD had been interests of engineers since its initiation in 1940s [1], e.g., propulsion systems [2,3], pumps [4,5], motors [6] and silicon growth [7]. More recently, MHD is also actively studied for the enhancement of heat transfer in conductive nanofluid flows [8–12]. The research for these practical applications mainly focused on the internal flow phenomena bounded by electric field where the Lorentz force is generated. In the meantime, the MHD jet flow driven by the Lorentz force is also an important issue in astrophysics [13,14] and atmospheric pressure plasma jet [15,16], in which the conductive medium is plasma.

On the other hand, the conventional jet flows, which neither electro nor magneto effects are involved, had been thoroughly investigated for decades, e.g., reviewed in Refs. [17,18]. The formation of turbulent jet is generally described as three main regions, i.e., the potential core, the developing region and the self-preservation region [19,20]. When the jet flow discharges immediately from the nozzle exit, the flow is mostly unperturbed to form a potential core. The region from the exit to the end of the potential core is also called the zone of flow establishment (ZFE). As interaction with the ambient fluid starts, the well-known Kelvin-Helmholtz instability emerges on the mixing layers. This region is referred to as the developing region. Significant turbulence is triggered in the developing region, and eventually results in the region of self-preservation, a state that the flow field can be solely determined by local behaviors. The developing region and the self-preservation region are commonly referred to as the zone of established flow. In addition, the Reynolds number (Re), given by $Re = VL/\nu$, had been well verified to dominate the development of flow regimes in two classic works [19,21]. Here, V, L and ν represent the jet exit velocity, the jet diameter and the kinematic viscosity of the discharge fluid, respectively. By visually inspecting the laminar length [19], fully laminar jet develops for $Re < 500$, while the laminar length completely disappears for $Re > 2500$. Determined by the turbulence dilution represented by temperature, a critical Reynolds number of $Re \approx 1500$ is quantitatively concluded [21]. Beyond this critical Reynolds number, dependence of the turbulence dilution on the Reynolds number is insignificant. Numerous follow-up studies regarding the role of the Reynolds number to the formation of jet flow had been presented in the last decades. For instance, the decay rate of the mean flow appears nearly independent on the Reynolds number for $Re \geq 10^4$ in a

* Corresponding author. Tel.: 886-3-5712121ext55125.
E-mail address: chingyao@mail.nctu.edu.tw (C.-Y. Chen).

https://doi.org/10.1016/j.jtice.2022.104369
1876-1070/

circular jet from a smoothly contracting nozzle [22]. The length of ZFE was experimentally confirmed to decrease with increasing Reynolds number for $Re \leq 5412$ [23]. Besides, the Reynolds number also plays an important role to the oscillatory behavior of mutually impinging jets in a mixing chamber. The frequency of the impinging jet oscillations is dictated by the Reynolds number, in which a transition regime occurs at $1500 < Re < 2000$ [24].

Another important issue studied intensively is the two phase jet, e.g., liquid jet associated with atomizing gas stream [25–27]. The coexistence of two phases, such as faster gas in a slower liquid jet, results in a shear instability on the interface, and forms a wavy stream. The wavy stream might further evolve into filaments, and eventually breaks into numerous droplets. When the atomization is incomplete, the breakup of liquid jet is non-axisymmetric with a wavelength larger than the jet diameter [25]. A flapping instability is recently observed in an incompletely atomized liquid jet, in which regime of the flapping instability is determined by the wavelength and liquid jet diameter [26]. Similar instability also occurs in an oscillating jet [28,29], such that the amplitude of oscillation is enhanced by the formation of a low pressure region near the leading edge of the deflected jet [29]. The control of self-sustained jet oscillations, which is highly relevant to the above literature, is important for many industrial applications, e.g., steel casting.

The MHD saltwater jet differs from the conventional liquid-gas jet by two features, i.e., driven by the Lorentz force and chemical reactions associated with electrolysis. It possesses potential applications to improve marine vehicle propulsion and hydrogen collection. In the present study, the products of reactions include gaseous bubble (hydrogen and oxygen) by water electrolysis and solid precipitates (aluminum hydroxide) from the aluminum electrodes. It is interesting to understand if the two-phase jet driven by the distinct Lorentz force evolves similarly with the conventional pressure-driven jet. Besides, unequal amount of gaseous bubbles are produced at electrodes, which provide perturbations. The perturbation might possibly lead to the jet oscillation. To our best knowledge, the influences of these factors to the MHD saltwater jet is rarely studied. In this paper, we focus on the pattern formation of the MHD jet. Parametric analysis is carried out, mainly by experiments, to identify transition of flow regime.

2. Physical problems and experimental apparatus

Magnetohydrodynamic (MHD) jet flows driven by the Lorentz force are studied. It is well known that the so-called Lorentz force is generated by perpendicularly oriented magnetic field and electric field, such that the force density, denoted as **F**, can be expressed as

$$\mathbf{F} = \mathbf{J} \times \mathbf{B}. \tag{1}$$

Here, **J** and **B** are current density and magnetic field, respectively. To experimentally study the MHD jet, the experimental apparatus is shown in Fig. 1. A pair of aluminum electrodes (drawn in blue), held by two acrylic plates (yellow) on their sides forming a 55mm-long open channel with width w in between, are placed inside a rectangular acrylic tank partially filled with saltwater of depth $h = 5$mm. The saltwater used in the experiments is the solution of distilled water and chemical salt, such that 35g salt is fully mixed in 1000ml water. Density and viscosity of this saltwater solution is $\rho = 1023\text{kg/m}^3$ and $\mu = 0.00097\text{N}\cdot\text{s/m}^2$, respectively. The electric conductivity of the saltwater is $\sigma = 5$ S/m measured by conductivity meter, where S stands for Siemens. A 40mm×20mm×10mm permanent NdFeB magnet (red) is placed right beneath the tank to provide an upward magnetic field **B**. Power suppliers are connected to the electrodes to generate an electric current **I** through the conductive saltwater and induce the Lorentz force **F**. The relation of current **I** and current density **J** is expressed as

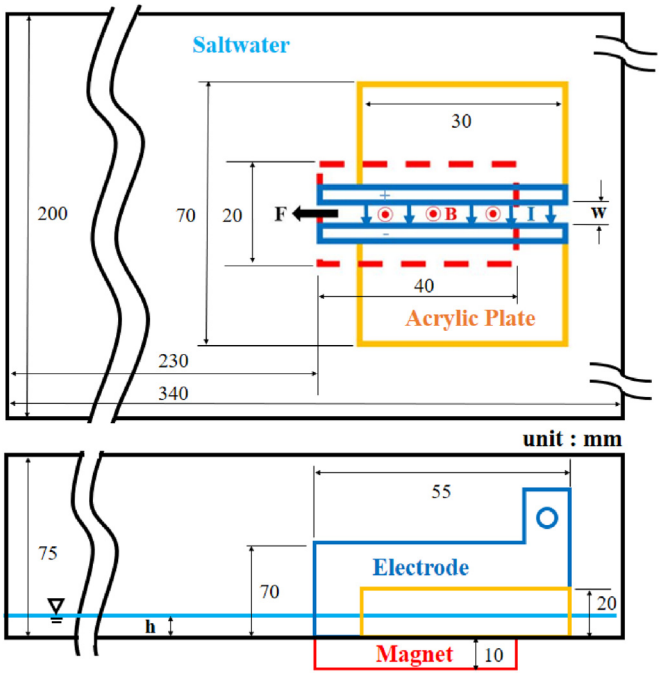

Fig. 1. Principle sketch of experimental apparatus: top and side view are shown on the top and bottom figures, respectively.

$$\mathbf{I} = \int_{A_c} \mathbf{J} dA. \tag{2}$$

Here, A_c is the area of cross-section perpendicular to current **I**. By this setup, the Lorentz force aligns with the axial direction of channel, denoted as x-direction as shown in Fig. 2, and drives a jet flow when the current presents. In the meantime, saltwater undergoes electrolysis, so that oxygen and hydrogen is generated at the anode and the cathode, respectively. It is noticed that, additional chemical reaction occurs on the aluminum electrodes, in which solid precipitates of aluminum hydroxide particles, i.e., $Al(OH)_3$, are produced. The overall reaction equation is

$$8H_2O + 2Al \rightarrow O_2 + +5H_2 + 2Al(OH)_{3(s)}. \tag{3}$$

The subscript (s) denotes solid precipitates. As a result, the volume of hydrogen produced at the cathode is 5 times higher than oxygen at the anode, which is experimentally confirmed by collecting the gases separately in a pure electrolysis without magnetic field. Aluminum hydroxide precipitates, which are turbid particles, are also visibly observed. It is noteworthy that, the much higher volume of hydrogen produced at the cathode significantly affects the jet formation for relatively lower current strength, which will be presented in the latter sections.

The magnetic field **B** generated by the permanent magnet can be predicted by the Maxwell equation, i.e., $\nabla \cdot \mathbf{B} = 0$. It is numerically solved by the commercially available software ANASYS Maxwell, and shown in Fig. 2 is the simulated result on the bottom plane of the tank. To better illustrate the position, an $x - y$ coordinate, whose origin is located at the center of the channel exit, is defined as marked in Fig. 2. By this coordinate, the channel is located at $-55\text{mm} \leq x \leq 0\text{mm}$ (length) and $-w/2 \leq y \leq w/2$ (width), while the position of magnet is at $-40\text{mm} \leq x \leq 0\text{mm}$ (length) and $-10\text{mm} \leq y \leq 10\text{mm}$ (width). Within the central region above the magnet, i.e., $-30\text{mm} \leq x \leq -10\text{mm}$, the field strength varies insignificantly with a maximum of $B \approx 0.19$T. Beyond this region, the strength decays rapidly. Also shown in Fig. 2 is the field distribution along the centerline of the channel, i.e., $y = 0$ and $-55\text{mm} \leq x \leq 0\text{mm}$. The measured field strength by Gauss meter along the channel is also shown for

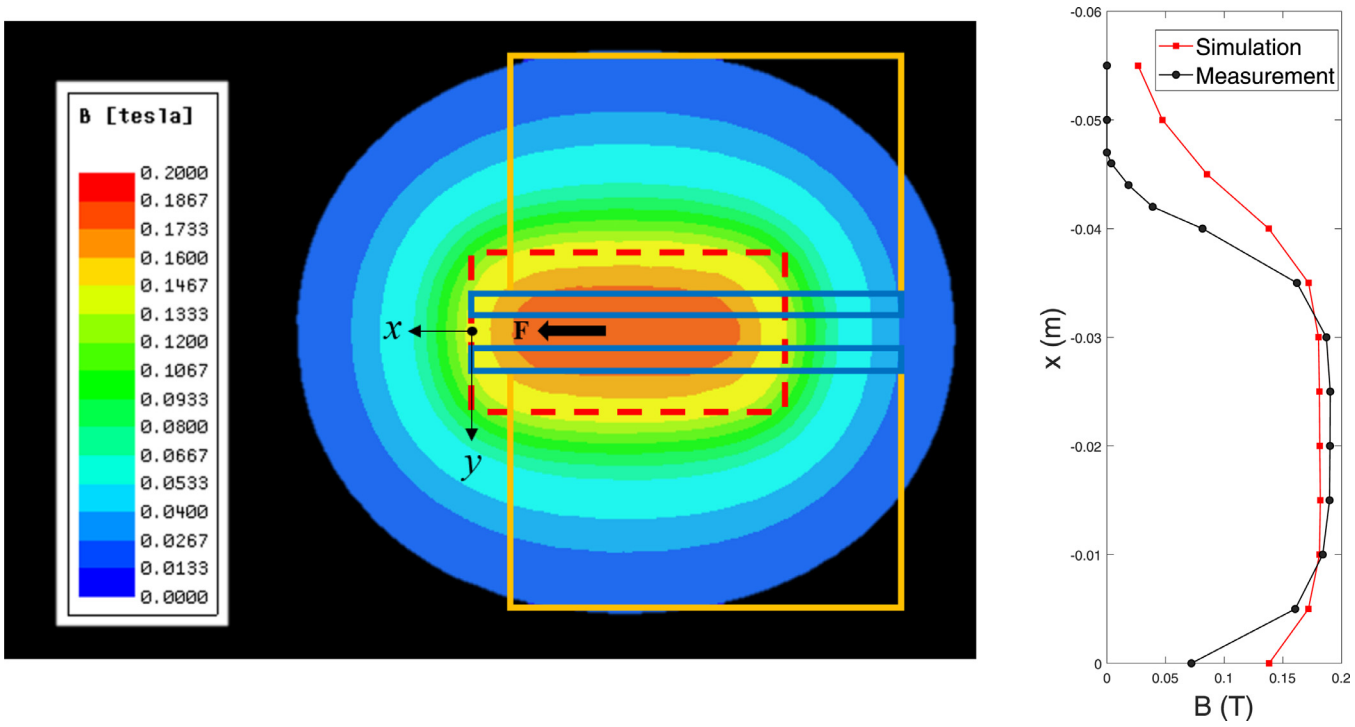

Fig. 2. Left: Numerical simulation of magnetic field strength. The positions of magnet, electrodes and acrylic plates referred in Fig. 1 are also drawn. Right: Comparison of measured magnetic strength with numerical result along the center line of the channel,.i.e., $y = 0$ and $-0.055 \leq x \leq 0$m. Fairly Good agreement is obtained.

comparison. Fairly good agreement is obtained between the numerical simulation and the actual measurement. We take the average of measured field strength of $B_0 = 0.147$T within the length covered by magnet (-40mm $\leq x \leq 0$mm) as a representative strength for the latter analysis.

Productions of gases and solid precipitates result in the present problem a typical multiphase flow. To visualize the jet pattern, we take advantage of the motion of gaseous bubbles, i.e., the bubbly jet, to represent the formation of MHD jet flow. When the Lorentz force is generated by electric current and magnetic field, top view ($x - y$ plane) of the bubbly jet flow is recorded by a CCD camera (GoPro Action with a fame speed of 60 fps) placed at the exit of the open channel. The pictures taken are imported into the Matlab software to further enhance the contrast, and presented in the latter sections. New saltwater solution is used in every experiment to ensure the same conductivity of the electrolyte.

3. results and discussion

In this study, the pattern formation of MHD bubbly jet is presented and discussed. Important parameters to the jet flow, including current strength I and channel width w, are varied to evaluate their effects.

3.1. Pattern formation

The MHD bubbly jets, represented by motion of oxygen and hydrogen produced respectively at the anode (top electrode) and the cathode (bottom electrode), are firstly presented in a series of experiments with increasing current strength I for $w = 4$mm. Shown in Fig. 3 is the experimental snapshots of $I = 1$A. Under the present condition of relatively weak Lorentz force, i.e., low electric current, mixing of the produced gases at early time is insignificant, so that two apparent layers, i.e., top oxygen layer and bottom hydrogen layer, are distinguishable inside the main structure of jet. As a result, the top and bottom interfaces of bubbly jet are mainly oxygen-saltwater and hydrogen-saltwater interface, respectively, and referred to as the oxygen interface and the hydrogen interface hereafter. At $t = 1.73$s shown in Fig. 3(a), a pair of counter-rotating vortices are formed at the front of jet by these two interfaces. Because of the unequally produced amount and different molecular weights of oxygen and hydrogen, the vortex pair results in an asymmetric bow-shaped front as shown at $t = 3.47$s shown in Fig. 3(b). In the meantime, the gaseous bubbles float upward to saltwater/air surface because of gravity. These bubbles are no longer visible once they escape from the saltwater. This explains the fewer amount of bubbles (represented by weaker brightness of image) at the downstream, especially for the hydrogen interface, where hydrogen is much lighter than oxygen. The jet appears as a slim, wavy, laminar and continuous bubbly stream at $t \geq 5.20$s shown in Fig. 3(c). It is noticed that, the pattern of wavy jet shown in Fig. 3 resembles the results reported in the literatures, e.g., experiments in incompletely atomized liquid jet [25] and simulations of spatially oscillating planar two-phase liquid jet [29]. The pattern resemblance suggests that production of unequal amount of oxygen and hydrogen results in an effect similar with incompletely atomization or spatial perturbation. For the case of stronger Lorentz force of $I = 4$A shown in Fig. 4, the main body of jet is much thicker due to larger amount of gases produced. The jet is strongly dispersive forming a bubbly stream with significant oscillation, i.e., shorter wave length and larger amplitude, at its upstream near the exit. On the other hand, typical turbulent feature of jet breakup evolves at farther downstream. As a result, similar with the conventional jet, the formation of the present MHD bubbly jet can be categorized into two regions by visual observation, i.e., (I) laminar bubbly stream near the exit, and (II) turbulent breakup at farther downstream. The length of nearly continuous laminar bubbly stream, denoted as L_c, is cutoff because of the downstream breakup.

The flows presented above indicate the evolution of jet from fully laminar bubbly stream to partially turbulent breakup by increasing the Lorentz force. A Reynolds number, the dimensionless parameter determining the tendency toward turbulence, based on the control input parameters is proposed to determine the transition. If length, time, velocity and pressure are scaled by D_H, $\sqrt{\frac{\rho D_H{}^3}{B_0 I}}$, $\sqrt{\frac{B_0 I}{\rho D_H}}$, and $\frac{B_0 I}{D_H}$,

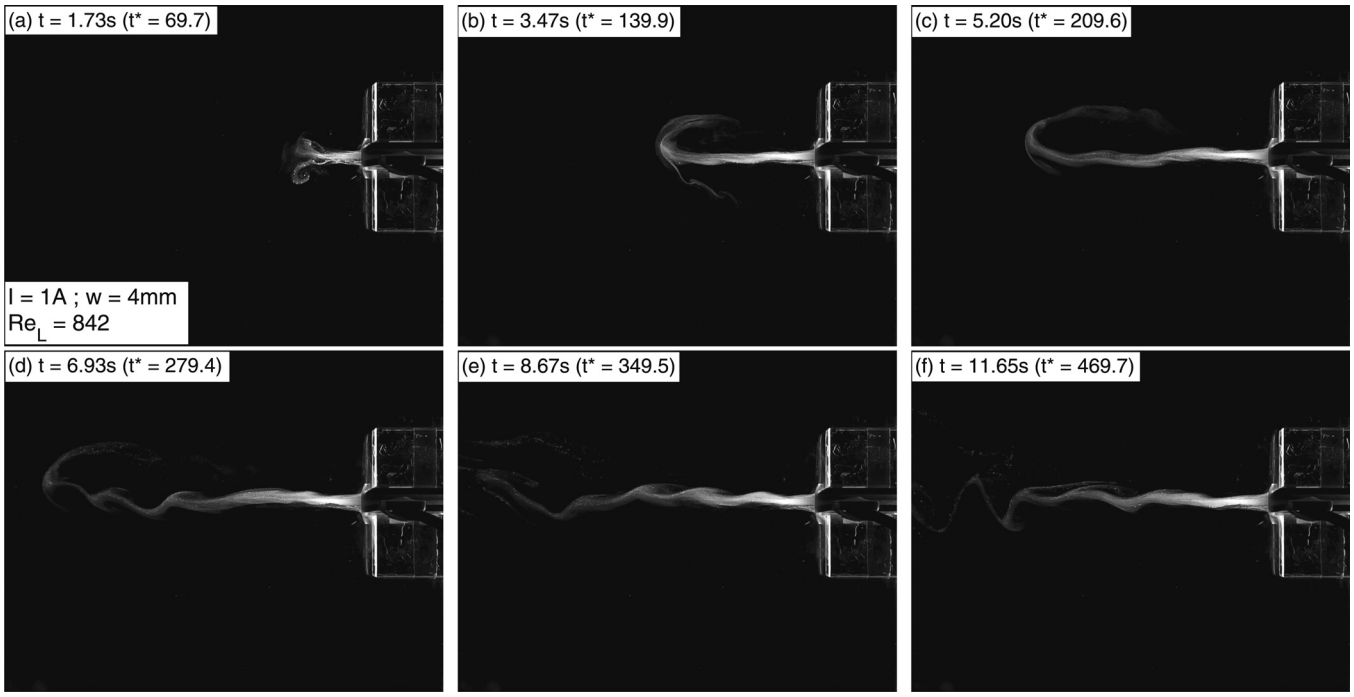

Fig. 3. Temporal evolution of MHD bubble jet for $I = 1$A, $w = 4$mm and $h = 5$mm, whose correspondent Reynolds number defined by (3.4) is $Re_L = 842$. The top-viewed images shown are mainly the gaseous bubbles, including oxygen and hydrogen respectively generated at the anode (top electrode) and the cathode (bottom electrode), by electrolysis of saltwater. The overall formation of bubble jet remains laminar.

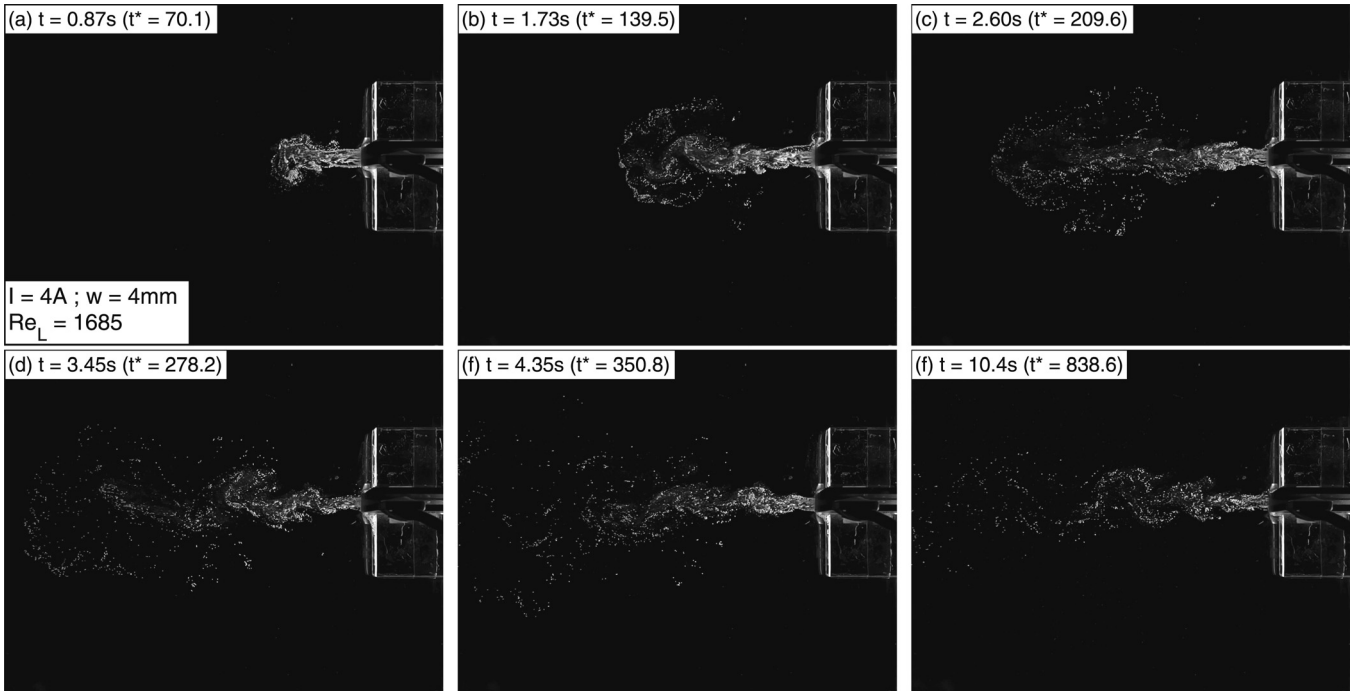

Fig. 4. Temporal evolution of MHD bubble jet for $I = 4$A, $w = 4$mm and $h = 5$mm ($Re_L = 1685$). Turbulent breakups are triggered at farther downstream.

respectively, the Reynolds number based on the Lorentz force Re_L is defined as

$$Re_L = \frac{\sqrt{\rho B_0 D_H I}}{\mu}. \tag{4}$$

Here, D_H is the hydraulic diameter of the channel. The dimensionless time t^* and length x^* are obtained accordingly as $t^* = t/\sqrt{\frac{\rho D_H{}^3}{B_0 I}}$ and $x^* = x/D_H$, respectively. By the scaling, the jets presented in Figs. 3 and 4 correspond to Re_L =842 and 1685, respectively. It is noticed that, the images shown in Fig. 3(a-e) and Fig. 4(a-e) are at about the same dimensionless times t^* for direct comparison. The longest visible positions of jet front at the downstream, denoted as x_F, are very close at near dimensionless times for all the cases. As expected, the jet flow evolves from fully laminar bubbly stream at low $Re_L = 842$ to turbulent breakup for a sufficiently high $Re_L = 1685$. For an even higher $Re_L = 2064$ ($I = 6$A) as shown in Fig. 5, in which the image is taken when $x_F \approx 165$mm, L_c is greatly shortened because of strong

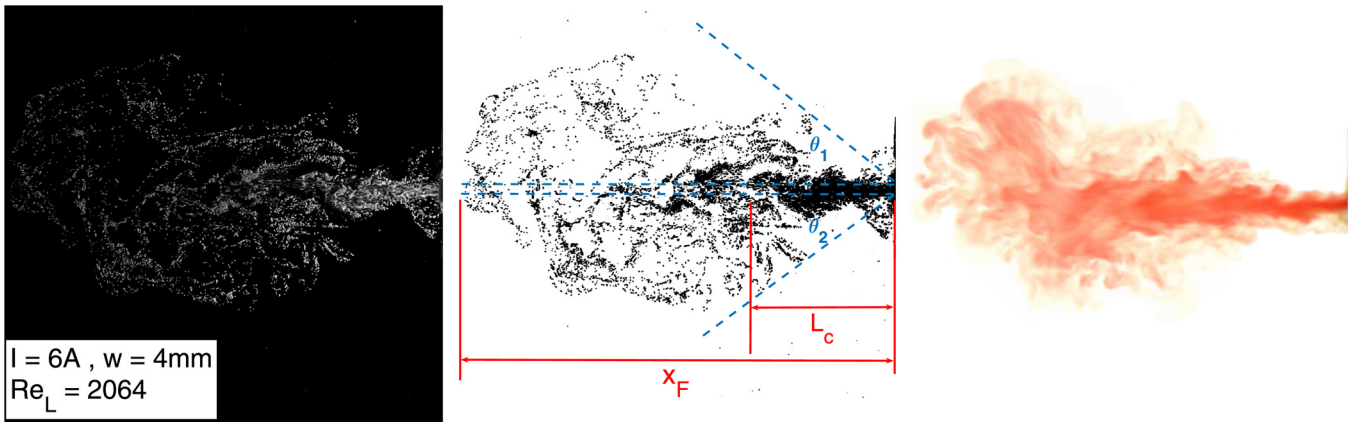

Fig. 5. (Left) Highly turbulent MHD bubble jet of $I = 6$A, $w = 4$mm and $h = 5$mm ($Re_L = 2064$). (Middle) Correspondent binary image indicating the length of continuous gaseous stream (L_c) and spread angles (θ_1 and θ_2). (Right) Image of red-dyed experiment with the same experimental parameters.

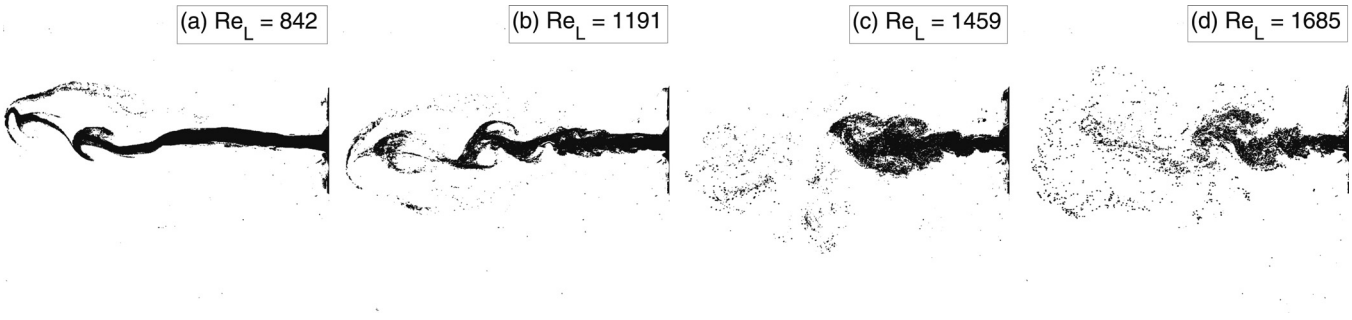

Fig. 6. Binary images of $I = 1$A ($Re_L = 842$), 2A ($Re_L = 1191$), 3A ($Re_L = 1459$) and 4A ($Re_L = 1685$). Shorter continuous gaseous stream (L_c) associated with larger total spread angle ($\theta = \theta_1 + \theta_2$) for higher current strength (or Re_L) is observed.

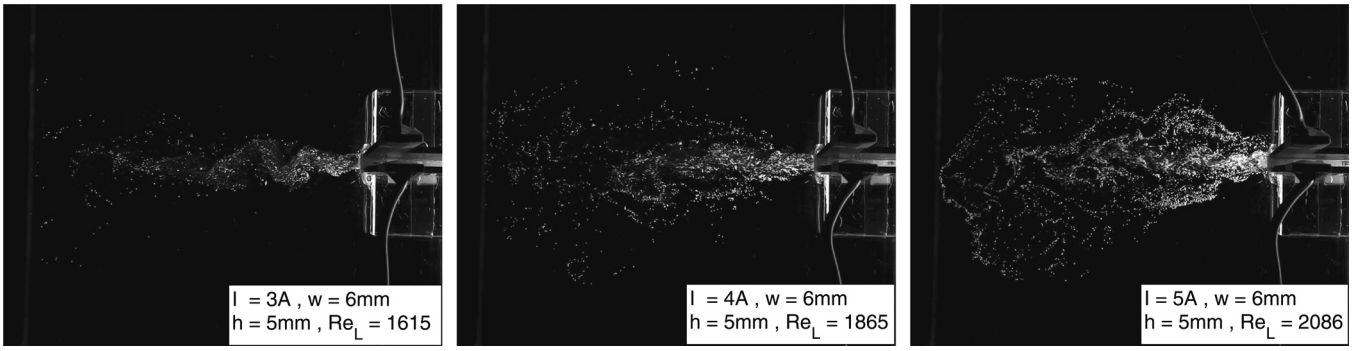

Fig. 7. Jet formation of wider channel $w = 6$mm and $h = 5$mm for various $I = 3$A ($Re_L = 1615$), 4A ($Re_L = 1865$) and 5A ($Re_L = 2086$).

turbulent breakup. Besides, the spreading area of gaseous bubbles is dramatically increased.

Another important issue is the appropriateness of the above visualization, based on bubbly stream, to represent the jet formation. The bubbles float vertically toward the saltwater surface because of buoyance, so that numerous bubbles will eventually disperse into the air once they reach beyond the water surface. The prominence, or brightness, of jet formation is expected to be weaker at farther downstream. In addition, bubbles might burst or coalesce. These phenomena result in much fewer bubbles remained in the downstream region. The jet flow by the conventional red-dyed saltwater for the highly turbulent case of $Re_L = 2064$ is also shown in Fig. 5. Overall pattern of the red-dyed jet shows strong similarity with the image represented by bubbly stream. It is noticed that, the red-dyed jet flows of various current strengths, e.g., $I = 1 \sim 6$A, have all experimented, and similar patterns with bubbly jets are confirmed.

To more easily identify some interesting phenomena of MHD jets, the original bubble image of $Re_L = 2064$ is converted to binary format by Matlab as also shown in Fig. 5. More binary images of lower current strengths taken when $x_F \approx 165$mm are demonstrated in Fig. 6, i.e., $Re_L = 842$, 1191, 1459 and 1685. It can be seen that the conversion to binary format accurately preserves the main pattern of bubbly jet. Consequently, useful quantitative measures, such as the length of continuous gaseous stream L_c and the spreading angles, top and bottom angle respectively denoted as θ_1 and θ_2 and depicted in Fig. 5, can be obtained. It is noticed that, no exact value of L_c can be determined considering the dispersive nature of bubbles. We first calculate the bubble density, represented by number of dark pixel in the binary image, along the jet. The length of L_c is then approximated when the bubble density drops dramatically. By visually inspecting these binary images, flow transition to trigger turbulent breakup by increasing Re_L is qualitatively categorized. For cases of $Re_L \leq 1191$, the jet formation appears a nearly continuous bubbly stream. Even

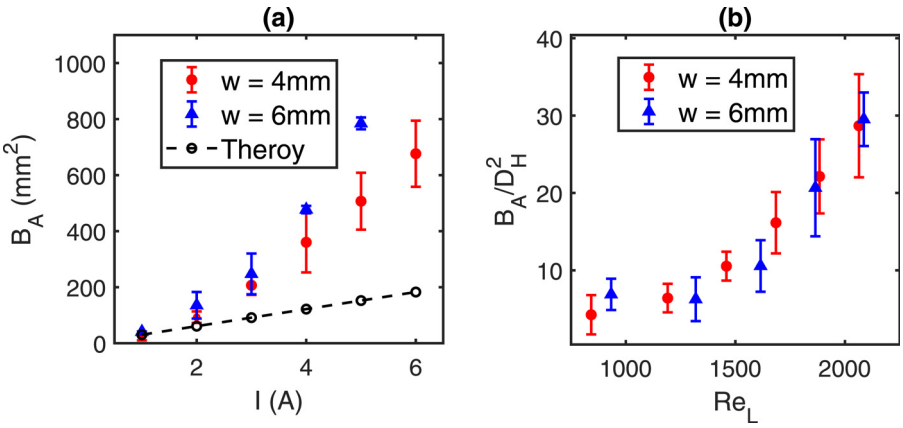

Fig. 8. (a) Areas occupied by gaseous bubbles B_A measured at $t = 1$s for various current strength I, and (b) dimensionless bubble area B_A/D_H^2 obtained at $t^* \approx 70$ versus Re_L. The growth of dimensionless bubble area is much higher for $Re_L > 1500$.

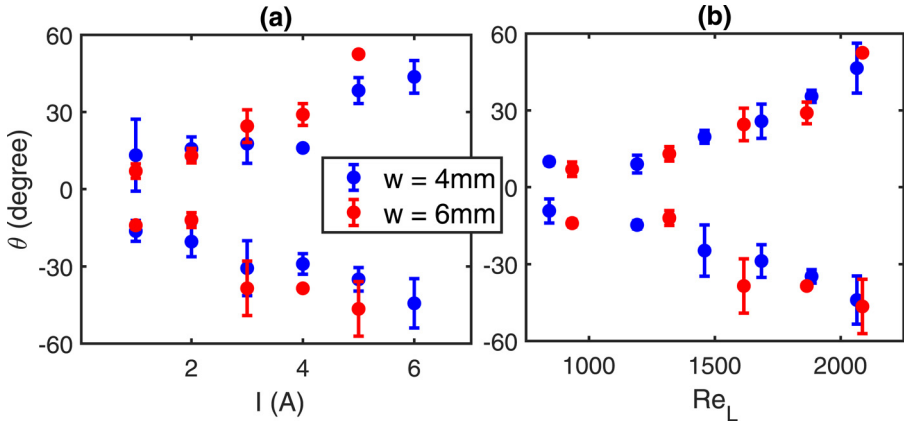

Fig. 9. (a): Spread angles θ of MHD bubble jet at $x_F \approx 165$mm for various current strength I, and (b) θ versus Re_L at dimensionless position of $x^* \approx 30$. The growth of θ shows rapid increase for $Re_L > 1500$.

apparent oscillation occurs at the downstream region, the flow remains laminar. If the Reynolds number is increased to $Re_L \geq 1459$, chaotic turbulent breakup evolves at downstream, while oscillation of the remaining laminar bubbly stream at upstream is more significant. A general trend of shorter L_c associated with larger total spread angle $(\theta_1 + \theta_2)$ for larger Re_L is confirmed. It is noteworthy the transition of turbulent breakup occurs at $Re_L \geq 1459$ is closed to the critical value of $Re = 1500$ reported in Ref. [19]. More discussion regarding the quantitative analysis of the flow transition will be presented in latter sections.

Change of channel width w results in different hydraulic diameter D_H, so that the correspondent Re_L is altered. It is expected that the jet would behave more unstable for a wider w if the rest of parameters remain unchanged. The jet formation of $I = 3$A ($Re_L = 1615$), 4A ($Re_L = 1865$) and 5A ($Re_L = 2086$) with $w = 6$mm are shown in Fig. 7. Turbulent breakup starts to evolve for $Re_L = 1615$ at downstream . The turbulent breakup is more prominent for the cases of $Re_L = 1865$ and 2086, which is consistent with the observation described in the above paragraphs. It is interesting to compare the cases of close Reynolds number but different combination of control parameters, e.g., $Re_L = 1685$ (Fig. 4d) and 1615 (Fig. 7), $Re_L = 2064$ (Fig. 5) and 2086 (Fig. 7). The jet formation for these two pairs of close Re_L appears very similarly. The pattern similarity supports the appropriateness for applying the proposed Reynolds number based on Lorentz force to consider the pattern formation of MHD jet. Flow transition, i.e., downstream turbulent breakup, occurs at a critical Reynolds number of $Re_L \approx 1500$.

3.2. Quantitative analysis

In this section, we turn to more quantitative analysis to the MHD bubbly jet. The first measure presented in Fig. 8(a) is the observed bubble area B_A at a representative time of $t = 1$s for various I. To obtain the area, number of dark pixel of the binary image is first counted, and converted to area. On the other hand, the bubbles, including oxygen and hydrogen, are produced by the water electrolysis, so that the amount can be calculated by the total electricity applied. If the gas is assumed to fully occupy the channel, the theoretical area is also shown in Fig. 8(a) as a reference. Fairly good agreement is obtained for sufficiently weak current strength of $I = 1$A. Because of the buoyancy and dispersion, bubbles spread and flow upward, so that the observed B_A is much larger than the theoretical prediction for $I \geq 2$A. The B_A grows much more rapidly for increasing I, despite of a liner proportionality by theoretical prediction. B_A for wider $w = 6$mm is generally larger than the cases of $w = 4$mm, which reflects stronger flow dispersion to enhance the spread of bubbles. To obtain a more general behavior of observed bubble area, dimensionless results are shown in Fig. 8(b). The dimensionless area, measured at an identical dimensionless time $t^* \approx 70$ and scaled by D_H^2, is plotted versus Re_L. The dimensionless area appears a nearly monotonic growth with Re_L. In addition, the growth increases rapidly for $Re_L > 1500$, which indicates flow transition to turbulence of strong dispersion.

Another measure of interest is the spreading angle θ, i.e., the top spreading angle θ_1 and the bottom spreading angle θ_2 as indicated in Fig. 5. To make direct comparison, all the measures are taken at

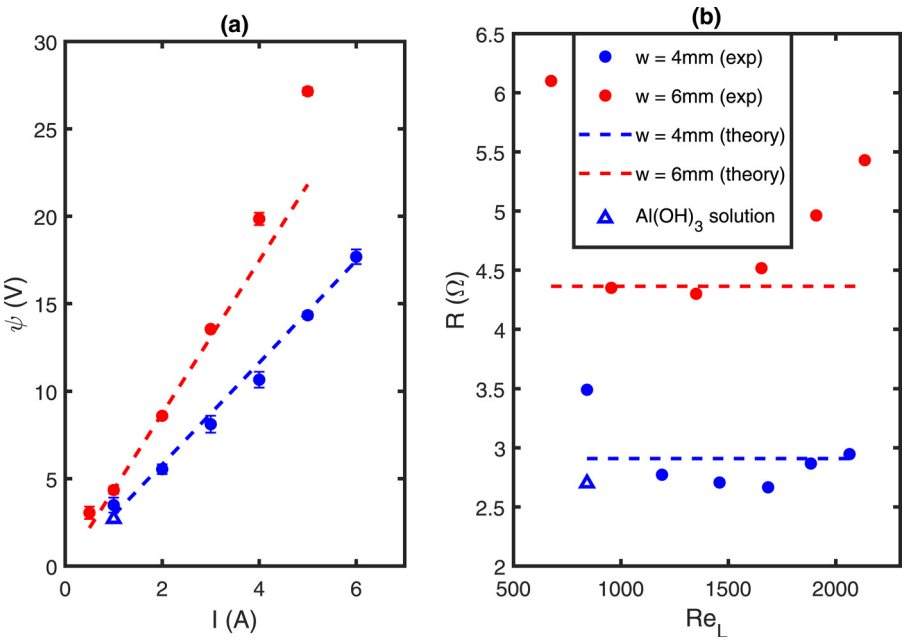

Fig. 10. (a) Applied electric potential ψ for various current strength I, and (b) effective electric resistance R versus Re_L. Theoretical values predicted by the Ohm's Law are also shown by dash lines.

$x_F \approx 165$mm as the sample images shown in Figs. 5 and 6. As shown in Fig. 9(a), the spreading angles are widened as the current strength is raised. The top and bottom spreading angle appears nearly symmetric for higher current strengths, which indicates the pattern is mainly dominated by flow rather than the local production of gases. The spreading angle for $w = 6$mm is generally wider than the case of $w = 4$mm under the same I. If θ is plotted versus the Re_L at an identical dimensionless position at $x^* \approx 32$ as shown in Fig. 9(b), monotonic increase with Re_L is nearly maintained. The θ also starts to show a rapid growth for $Re_L \approx 1500$. Overall, the dependence of θ on Re_L is similar with dimensionless B_A shown in Fig. 8(b), which suggests the transition of flow regime is dominated by Re_L and strong turbulent breakup is triggered at $Re_L \approx 1500$.

Before concluding this section, we discuss an interesting effect of the solid precipitates of $Al(OH)_3$. When considering the MHD applications, the input power is an important factor often discussed. In the present study, the direct control parameter is current strength I (or current density). Since gases and precipitates are produced, the conductivity of the solution would not be the same as the pure saltwater. As a result, the applied electric field, represented by the electric potential ψ, can be roughly used to assess the effect of individual component. Production of gaseous bubbles increases the total electric resistance of solution, so that the applied electric potential to maintain the same current strength is expected higher than the case of pure saltwater. The actual electrical potential ψ applied to maintain constant current strength I is plotted in Fig. 10(a). The potential needed for the case of pure saltwater, whose linear dependence can be obtained theoretically by the Ohm's Law, such as $\psi = Iw/\sigma A_c$, is also shown for comparison. As expected, higher potential is needed for a wider channel of $w = 6$mm because of more amount of saltwater between the electrodes. It is interesting to notice that, the applied potential ψ appears slightly lower than the theoretical value for intermediate current strength, e.g., 2A $\leq I \leq$5A and 1A $\leq I \leq$2A for $w = 4$mm and 6mm, respectively. Only for sufficiently weak and strong current strength, higher potential than theoretical value is needed as one might expect. The reason for this inconsistent behavior is due to the presence of solid precipitate $Al(OH)_3$. Since $Al(OH)_3$ is more conductive than saltwater, so that production of $Al(OH)_3$ could reduce the overall electric resistance. To confirm the effect of $Al(OH)_3$, a reference experiment of $I = 1$A and $w = 4$mm is performed by using saltwater solution originally containing $Al(OH)_3$. As also shown in Fig. 10, the potential needed and the correspondent resistance, obtained by the Ohm's Law, is lower than the experiment of pure saltwater, which confirms the enhancement of conductivity by $Al(OH)_3$.

According to the above results, two opposite effects compete to determine the needed electrical potential, e.g., conductive solid precipitates and non-conductive gaseous bubbles. It can be seen in the reaction Eq. (3), the amount of conductive solid precipitate is less than the non-conductive bubbles. For conditions of weak current, the enhancement of resistance by bubbles in the channel prevails, so that the needed potential is higher. As the current is raised, more amount of bubbles are displaced out of the channel, either by the flux or buoyancy, than solid precipitates. As a result, the effect of conductive solid precipitates becomes more significant to reduce the needed potential. However, for an even stronger current, turbulent flow evolves. The chaotic turbulent flow may trap the bubbles inside the narrow channel more easily, so that the effective resistance starts to rise again. The resistance R in different Re_L is plotted in Fig. 10(b) to realize the inconsistent behavior affected by flow regime. R is initially higher than the pure saltwater for $Re_L < 1000$, and decreases for higher Re_L. Nevertheless, R reverses to rise for $Re_L = 1500 \sim 1600$, which is in line with the change of flow pattern presented above.

4. Conclusion

Pattern formation and flow transition of magnetohydrodynamic (MHD) bubbly jet driven by the Lorentz force in conductive saltwater is studied. The Lorentz force generated by perpendicularly placed magnetic field and electric field displaces the saltwater in an open channel bounded by the two plates of aluminum electrodes. In the meantime, chemical reactions take place to produce gaseous bubbles (oxygen and hydrogen) and solid precipitates (aluminum hydroxide). The displaced flux of the saltwater/bubbles/precipitates solution into the ambient saltwater forms a typical three-phase MHD jet flow. Taking advantage of the brightness of gaseous bubble, the pattern of jet flow is mainly represented by the bubbly flow recorded directly. Flow transition from laminar to turbulent is categorized.

The Lorentz force is directly proportional to the current density, so that a representative series of experiments, by varying the input electric current strength, is firstly presented to illustrate the jet flow affected by the Lorentz force. By raising the current strength, pattern of MHD bubbly jet evolves from a slightly wavy, nearly continuous, laminar gaseous stream toward chaotic turbulent flow, which meets common expectation. A new Reynolds number Re_L, based on the Lorentz-force and defined by the strength of magnetic field and electric current, is proposed to categorize the flow regime. Turbulent breakup starts to evolve once the Re_L exceeds a critical value at $Re_L \approx 1500$. Dependence of relevant quantitative measures, e.g., spreading area, angles of bubbly jet and needed electric potential, on the control parameters are also studied. These dimensionless measures generally depend monotonically on the Re_L. Nevertheless, rapid growth of these measures occurs for the cases of $Re_L > 1500$, which indirectly confirms the transition of flow regime at $Re_L \approx 1500$.

Declaration of Competing Interest

Study the MHD bubbly jet experimentally.

Propose a new Lorentz-force based Reynolads number Re_L capable to demonstrate the pattern similarity, and determine the flow transition.

Verify the critical value of $Re_L \approx 1500$ to trigger turbulence breakup.

Acknowledgements

Supports by the Ministry of Science and Technology, Taiwan (MOST 110-2221-E-A49 -045 -MY3) is acknowledged.

References

[1] Alfven H. Existence of electromagnetic-hydrodynamic waves. Nature 1942;150:450.
[2] Cebron D, Viroulet S, Vidal J, Masson JP, Viroulet P. Experimental and theoretical study of magnetohydrodynamic ship models. PLoS ONE 2016;12:e0178599.
[3] Chan CS, Cheng JH, Zeng CH, Huang JR, Chen YH, Chen YJ, Pham Thi T, Chao WH, Jeng JT, Liu TL, Pan KC, Li YH, Chen CY. Design of marine vehicle powered by magnetohydrodynamic thruster. Magnetohydrodynamics 2020;56:51.
[4] Jang J, Lee S. Theoretical and experimental study of MHD (magnetohydrodynamic) micropump. Sensors and Actuators A: Physical 2000;80:84.
[5] Timofeev VN, Khatsayuk MY, Kizhaev IV. Mathematical simulation of electromagnetic and hydrodynamic processes in the MHD pump. Magnetohydrodynamics 2019;55:337.
[6] Haghparast M, Pahlavani M, Azizi D. Numerical investigation of the effects of magnetic field and fluid electrical conductivity on the performance of marine magnetohydrodynamic motors. IET Electric Power Applications 2018;12:1207.
[7] Lin CH, Chen PW, Chen CY. Simulations of silicon CZ growth in a cusp magnetic field. Magnetohydrodynamics 2011;47:17.
[8] Selimefendigil F, Oztop HF. Mixed convection of nanofluid filled cavity with oscillating lid under the influence of an inclined magnetic field. Journal of the Taiwan Institute of Chemical Engineers 2016;63:202–15.
[9] Ghadikolaei SS, Gholinia M, Hoseini ME, Ganji DD. Natural convection MHD flow due to $mos_2 - ag$ nanoparticles suspended in $c_2h_6o_2 - h_2o$ hybrid base fluid with thermal radiation. Journal of the Taiwan Institute of Chemical Engineers 2019;97:12–23.
[10] Hashim HA, Khan M. Multiple solutions for MHD transient flow of williamson nanofluids with convective heat transport. Journal of the Taiwan Institute of Chemical Engineers 2019;3:26–137.
[11] Alizadeha R, Mesgarpourb M, Americ A, Abadd J, Wongwisesb S. Artificial intelligence prediction of natural convection of heat in an oscillating cavity filled by cuo nanofluid. Journal of the Taiwan Institute of Chemical Engineers 2021;124:75–90.
[12] Zhanga L, Bhattia MM, Shahidb A, Ellahic R, Begd O, Saite SM. Nonlinear nanofluid fluid flow under the consequences of lorentz forces and arrhenius kinetics through a permeable surface: A robust spectral approach. Journal of the Taiwan Institute of Chemical Engineers 2021;124:98–105.
[13] Ferrari A. MODELING EXTRAGALACTIC JETS. Annu Rev Astron Astrophys 1988;36:539.
[14] Bellan PM. Experiments and models of MHD jets and their relevance to astrophysics and solar physics. Physics of Plasmas 2018;25:055601.
[15] Yuan MH, Chang CC, Chang CY, Lin YY, Shie JL, Wu CH, Tseng JY, Ji DR. Radio-frequency-powered atmospheric pressure plasma jet for the destruction of binary mixture of naphthalene and n-butanol with pt/al_2o_3 catalyst. Journal of the Taiwan Institute of Chemical Engineers 2014;45:468–74.
[16] Sar A., Shabani E., Haghighi M., Shabani M.. Synergistic catalytic degradation of ciprofloxacin using magnetic carbon nanomaterial/$nife_2o_4$ promoted cold atmospheric pressure plasma jet: Influence of charcoal, multi walled carbon nanotubes and walnut shell. Journal of the Taiwan Institute of Chemical Engineers, In press.
[17] Lasheras JC, Hopfinger EJ. Liquid jet instability and atomization in a coaxial gas stream. Annu Rev Fluid Mech 2000;32:275.
[18] van Hout R, Murugan S, Mitra A, Cukure B. Coaxial circular jets: A review. Fluids 2021;6:147.
[19] Pearce AF. Critical reynolds number for fully-developed turbulence in circular submerged water jets, council for scientific and industrial research. Report MEG 475, Pretoria, South Africa, August; 1966.
[20] Magstadt AS. Investigating the structures of turbulence in a multi-stream, rectangular. Supersonic Jet, Ph.D. Dissertation, Syracuse University, June; 2017.
[21] Ungate C, Harleman D, Jirka G. Stability and mixing of submerged turbulent jets at low reynolds numbers. Energy Laboratory Report No. MIT-EL75-014; 1975.
[22] Mi J, Xu M, Zhou T. Reynolds number influence on statistical behaviors of turbulence in a circular free jet. Physics of Fluids 2013;25:075101.
[23] Kwon SJ, Seo AW. Reynolds number effects on the behavior of a non-buoyant round jet. Experiments in Fluids 2005;38:801.
[24] Tomac MN, Gregory JW. Oscillation characteristics of mutually impinging dual jets in a mixing chamber. Phys Fluids 2018;30:117102.
[25] Farago Z, Chigier N. Morphological classification of disintegration of round liquid jets in a coaxial air stream. Atomization Sprays 1992;2:137.
[26] Delon A, Cartellier A. Flapping instability of a liquid jet. Physical Rev Fluids 2018;3:043901.
[27] Xiong P, He S, Qiu F, Cheng Z, Quan X, Zhang X, Li W. Experimental and mathematical study on jet atomization and flash evaporation characteristics of droplets in a depressurized environment. Journal of the Taiwan Institute of Chemical Engineers 2021;123:185–98.
[28] Schmidt S, Kruger O, Gockeler K, Paschereit CO. Numerical investigation of the breakup behavior of an oscillating two-phase jet. Phys Fluids 2018;30:072101.
[29] Arote A, Bade M, Banerjee J. Numerical investigations on stability of the spatially oscillating planar two-phase liquid jet in a quiescent atmosphere. Phys Fluids 2019;31:112103.